nature nanotechnology

ARTICLES

https://doi.org/10.1038/s41565-021-00998-x

Steam disinfection releases micro(nano)plastics from silicone-rubber baby teats as examined by optical photothermal infrared microspectroscopy

Yu Su[1], Xi Hu[2], Hongjie Tang[2], Kun Lu[1], Huimin Li[1], Sijin Liu[3], Baoshan Xing[4]✉ and Rong Ji[1]✉

Silicone-rubber baby teats used to bottle-feed infants are frequently disinfected by moist heating. However, infant exposure to small microplastics (<10 μm) potentially released from the heated teats by hydrothermal decomposition has not been studied, owing to the limitations of conventional spectroscopy in visualizing microplastic formation and in characterizing the particles at the submicrometre scale. Here both the surfaces of silicone teats subjected to steam disinfection and the wash waters of the steamed teats were analysed using optical-photothermal infrared microspectroscopy. This new technique revealed submicrometre-resolved steam etching on and chemical modification of the teat surface. Numerous flake- or oil-film-shaped micro(nano)plastics (MNPs) (in the size range of 0.6–332 μm) presented in the wash waters, including cyclic and branched polysiloxanes or polyimides, which were generated by the steam-induced degradation of the base polydimethylsiloxane elastomer and the polyamide resin additive. The results indicated that by the age of one year, a baby could ingest >0.66 million elastomer-derived micro-sized plastics (MPs) (roughly 81% in 1.5–10 μm). Global MP emission from teat disinfection may be as high as 5.2×10^{13} particles per year. Our findings highlight an entry route for surface-active silicone-rubber-derived MNPs into both the human body and the environment. The health and environmental risks of the particles are as yet unknown.

Microplastic (<5 mm) pollution is a current global concern as it may pose environmental as well as health risks[1–5]. Humans take up microplastics derived from plastic waste and products in use[6–9]. The latter route can expose humans to large quantities of microplastics over the long term and directly[8,9]. Most studies of direct human exposure have focused on petroleum-based thermoplastics (for example, polyethylene terephthalate (PET) and nylon)[7], whereas elastomers such as silicone rubber, an environmental source of microplastics[10,11], have yet to be considered. Silicone rubber, prepared via the Pt-catalysed hydrosilylation crosslinking of polydimethylsiloxane (PDMS) chains[12] (Supplementary Fig. 1), is a common material for baby bottle teats[13]. The World Health Organization recommends disinfecting the teats by commercial steam disinfector or boiling water before each feeding[14]. Nonetheless, silicone rubber may decompose at elevated temperatures[15,16], catalysed by trace amounts of the Pt residues[17]. Furthermore, silicone teats contain hot melt adhesives, such as polyamide (PA) resin[18], which can also decompose during moist heating. Yet, whether the moist heat disinfection of silicone teats produces micro-sized plastics (MPs) (1–1,000 μm) and nanoplastics (NPs, <1 μm), analogous to thermoplastic weathering and fragmentation processes[19–21], is unknown. Infants are sensitive and vulnerable to contaminants[22], therefore their exposure to MNPs (<1,000 μm) through bottle feeding must be evaluated, which is essential for protecting infant health[9].

Generally, assessments of human exposure to microplastics have not included small microplastics, potentially more toxic NPs[5]. Also, previous work has not investigated the chemical mechanisms underlying the formation of micro(nano)plastics (MNPs)[8,9], largely due to inadequate analytical methods. For instance, classical Fourier-transform IR (FTIR) and Raman microspectroscopy, the most-frequently used methods for chemical identification of microplastics in environmental samples[23–25], can examine particles with sizes only down to a few micrometres in practice due to the limited spatial resolution and sample fluorescence interference[26–28] (details in Supplementary Note 1 and Table 1). This highlights the need for new approaches to characterizing MNPs at the submicrometre scale to obtain a detailed understanding of their formation, exposure and thus risks to human and environmental health.

optical-photothermal infrared (O-PTIR) microspectroscopy is a still-emerging technique, designed for (3D-)imaging living cells and organisms[29], which uses a continuous-wave visible-laser probe to detect the photothermal response of the mid-IR-absorbing regions of a sample (schematic diagram in Fig. 1a) and thus does not require sample contact[29,30]. This pump-probe mechanism improves the spatial resolution (roughly 400 nm)[30] and sensitivity (roughly 0.4 pg)[31] in O-PTIR compared with those of FTIR (for example, 3.4–13.5 μm and 100 pg in transmission mode[28,32]) and allows O-PTIR to be free of sample fluorescence interference (Supplementary Table 1). These features of O-PTIR can fulfil both submicrometre-resolved imaging of individual MNPs and depth-resolved determination of the chemically modified polymers that make up those particles. However, O-PTIR has yet to be used to trace the formation of MNPs.

Here we first validated the performance and applicability (including the spectral fidelity, reproducibility, resolution and sensitivity) of O-PTIR, using a commercial microspectroscope to test multiple thermoplastics (details in Supplementary Note 2). An excellent consistency between the O-PTIR and FTIR spectra (around a 99% match rate for polystyrene (PS)) was demonstrated, together with excellent reproducibility of the O-PTIR spectra (±0.2% variability

[1]State Key Laboratory of Pollution Control and Resource Reuse, School of the Environment, Nanjing University, Nanjing, China. [2]Quantum Design (Beijing) Co., Ltd, Beijing, China. [3]State Key Laboratory of Environmental Chemistry and Ecotoxicology, Research Center for Eco-Environmental Sciences, Chinese Academy of Sciences, Beijing, China. [4]Stockbridge School of Agriculture, University of Massachusetts, Amherst, MA, USA. ✉e-mail: bx@umass.edu; ji@nju.edu.cn

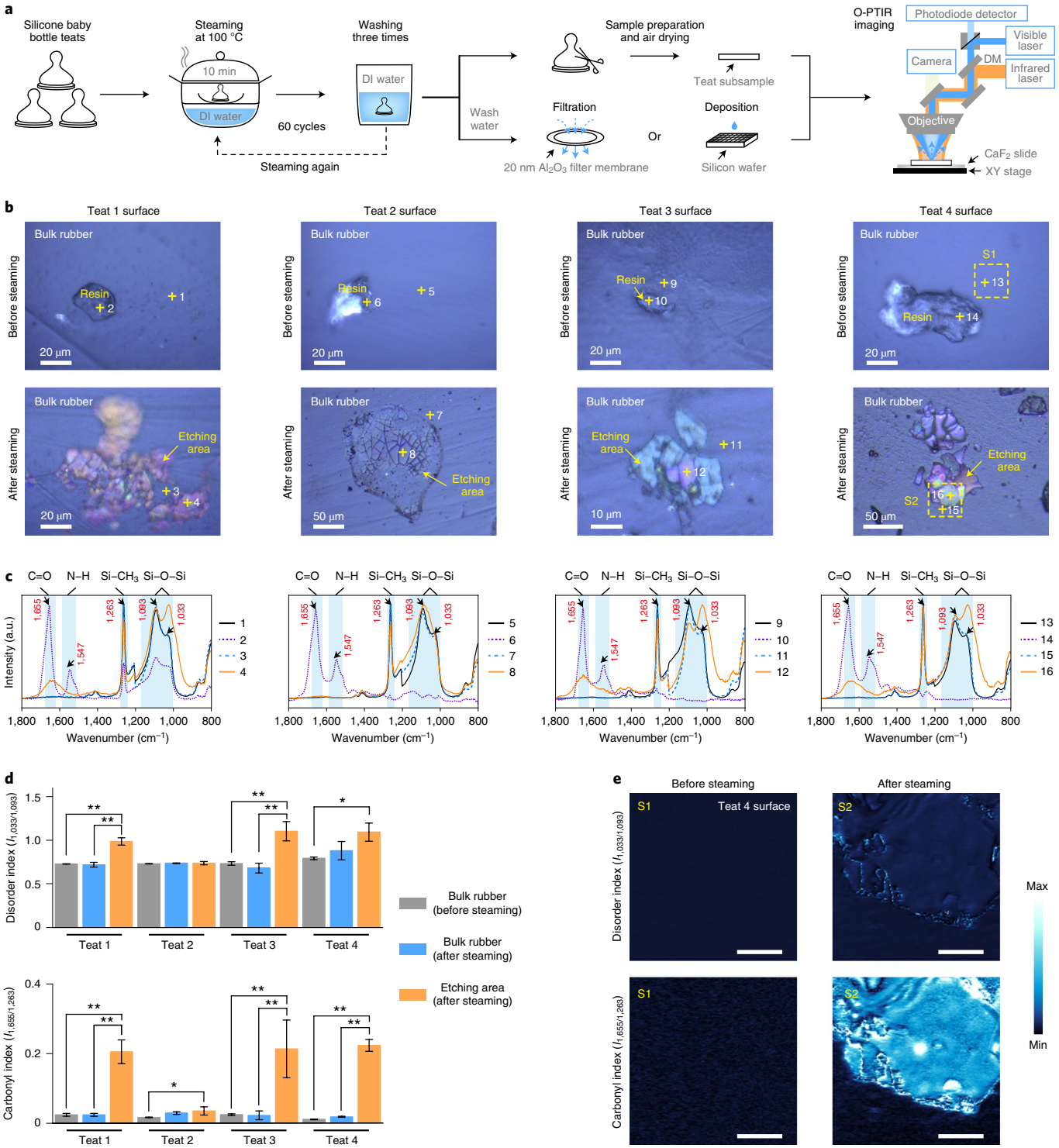

Fig. 1 | Steam etching of silicone-rubber teat surface by hydrothermal decomposition. a, Schematic of the experimental setup. New teats (brands 1–4) were repeatedly steamed for 10 min at 100 °C followed by DI water washing and air drying. Then, the teat subsamples and contents of wash waters were prepared for O-PTIR microspectroscopy imaging. The microspectroscope combined 532 nm visible and pulsed IR lasers collinearly through a dichroic mirror (DM); the laser beams were focused onto sample surface through a reflective objective; IR absorption caused thermal expansion that locally changed the propagation of the visible beam; the intensity of reflected visible laser was measured by a photodiode detector, which was synchronously demodulated to create IR absorption spectra and IR images were created by measuring the IR absorption while scanning the sample on an XY stage. A conventional optical microscope camera is equipped for selection of regions of interest for IR measurements. **b**, Optical images of teat subsample surfaces before and after 60 × 10 min of steaming. The arrows indicate the positions of resin particles and etching areas. **c**, Normalized O-PTIR spectra of positions 1–16 in **b**. a.u., arbitrary units. **d**, Ratios of IR absorption intensity ($I_{1,033/1,093}$, the disorder index; $I_{1,655/1,263}$, the carbonyl index) determined for the surface of the bulk rubber and etching areas. Data points are mean ± s.d. calculated from three random sampling points. Statistically significant differences were determined using ANOVA and Tukey's test; $^{*}P < 0.05$, $^{**}P < 0.01$. **e**, Ratio maps ($I_{1,033/1,093}$ or $I_{1,655/1,263}$) derived from the O-PTIR images of the regions S1 and S2 in **b**. The images were acquired at a resolution of 200 nm per point, a rate of 1,000 µm s^{-1}, a visible-laser power of 5%, an IR power of 8% and a detector gain of 5×. The colour scales show the signal intensity. Scale bars, 20 µm.

within a 5-μm change in the sampling spot) as well as the ability of the instrument to differentiate between the O-PTIR spectra of spots spaced 200 nm apart and to characterize thin samples (for example, a 200-nm-thick PET film) (Supplementary Figs. 2 and 3). Then, we successfully used the O-PTIR microspectroscopy to (1) visualize the hydrothermal decomposition of the base PDMS elastomer and PA resin additive of silicone teats during steam disinfection, (2) characterize the changes in the molecular structure of the MNPs released from the steamed teats, (3) reveal the mechanisms responsible for the formation of the particles and (4) quantitatively estimate both the intake of elastomer-derived MPs by bottle-fed infants and the emission of the particles to the environment. Our study shows that O-PTIR can be used to determine the environmental source and abundance of MNPs. It also indicates that steam-disinfected silicone teats are both a new route of human exposure to substantial numbers of MNPs and a source of environmental pollution. The risks to human and environmental health posed by the surface-active MNPs released from the disinfected silicone teats should therefore be investigated in further research.

Steam disinfection triggers polymer decomposition on silicone teats

While the heat resistance temperature (110–180 °C, according to the manufacturers) of four popular brands (denoted nos. 1–4) of silicone teats used in this study indicated that thermal decomposition occurs at a much higher temperature, we found etching of the teats by steam disinfection at 100 °C using O-PTIR microspectroscopy (experimental setup in Fig. 1a). From the optical images of randomly selected small regions on the teat surfaces (Fig. 1b), etching areas were clearly seen on the steamed teat surfaces, whereas the non-steamed teat surfaces were relatively smooth, indicating steaming-induced formation of the etching areas. O-PTIR spectra and images showed that repeated steaming (60 × 10 min) caused notable chemical modification of the silicone rubber on the teat surfaces. In the O-PTIR spectra of the teat samples before steaming, the presence of the characteristic bands of PDMS (Fig. 1c, points 1, 5, 9 and 13), including a symmetric Si–CH_3 deformation vibration (1,263 cm^{-1}) and a Si–O–Si asymmetric stretching vibration (1,093 and 1,033 cm^{-1})[33], indicated the similar molecular composition of the bulk rubbers of the four teats. All resin particles had the amide I (C=O stretching at 1,655 cm^{-1}) and II (N–H in-plane bending at 1,547 cm^{-1}) bands of PA (Fig. 1c, points 2, 6, 10 and 14), with some resins (for example, point 2) exhibiting additional bands characteristic of PDMS, consistent with the presence of PA or PDMS–PA polymer blends. After the 60th steaming, the widened Si–O–Si bands (Fig. 1c, orange versus blue lines) suggested the formation of longer, branched siloxane chains[34]. The disorder index ($I_{1,033/1,093}$), an indicative of a random network-like structure[35], on the etching areas of the teat samples (except teat 2) was significantly ($P < 0.05$) higher than the bulk rubbers (Fig. 1d), demonstrating that the transformation of PDMS into a relaxed disordered structure occurred on the etching area. Additionally, a C=O band at 1,655 cm^{-1} was detected on the etching areas but not on the bulk rubbers (Fig. 1c, orange versus blue lines), which was consistent with the significantly ($P < 0.05$) higher carbonyl index ($I_{1,655/1,263}$), indicative of the oxidation degree[36] on the etching areas of most teat samples (Fig. 1d), indicating that partial oxidation of the PDMS on the etching area to carbonyl-containing species (for example, Si–C–C=O)[34] occurred during the steaming. Due to the inductive effect of the Si–C group, the C=O stretching frequency was 10–20 cm^{-1} lower than that of its carbon analogue[37]. The maps of $I_{1,033/1,093}$ and $I_{1,655/1,263}$ (Fig. 1e) derived from the O-PTIR images showed clear differences in the intensity of chemical modification of the etching areas from the corresponding bulk rubbers after steaming (Fig. 1e, S2), different from the non-steamed teat surfaces (Fig. 1e, S1). These results demonstrated that the PDMS decomposed across the etching area surfaces.

Visualization of hydrothermal decomposition of silicone-teat polymers

The evolution of etching was visualized by O-PTIR microspectroscopy. Figure 2a shows the morphological changes at the same location on a subsample surface of teat 1 before and 10, 60 and 600 min after steaming (that is, the first, sixth and 60th 10 min steaming). Before steaming, a large number of resin particles randomly occurred on the relatively smooth bulk-rubber surface (Fig. 2b, S1). After 10 min of steaming, a micro-sized dent (length roughly 16 μm) and etching area (length roughly 88 μm) appeared on the subsample surface and a few cracks developed from the edge of the etching area (Fig. 2b, S2). After 1 h of steaming, the etching area fragmented, thereby allowing the underlying surface to form a new dent (Fig. 2b, S3). Rapid dent formation suggested the release of MPs and even NPs. After 10 h of steaming, the brightness of the etching area surface decreased (Fig. 2b, S4), which probably represented the increased decomposition of local PDMS. In agreement with the results obtained from the whole teats (Fig. 1d), the O-PTIR spectra of the subsample (Fig. 2c) showed increases in $I_{1,655/1,263}$ (2.9–6.2 fold) and $I_{1,033/1,093}$ (13–23%) of the etching area compared with the bulk rubber as the steaming time increased from 1 to 10 h. For the non-steamed teat subsamples, neither dents nor etching areas were found (Supplementary Fig. 4), demonstrating that steam etching accounted for the observed PDMS decomposition on the teat surface. As the total steaming time increased from 10 min to 10 h, the reflectivity of the visible laser from the etching area was largely reduced, whereas the intensity of the carbonyl band (1,655 cm^{-1}) in O-PTIR images at the same area gradually increased (Fig. 2d), indicating the formation of a rougher and higher oxidized surface of the etching area that was presumably due to the increased oxidative decomposition of PDMS. To confirm the oxidation of PDMS, teat 1 subsamples were examined using X-ray photoelectron spectroscopy (XPS), but the differences in the XPS spectra and O/C ratios of the subsamples before and after steaming were not significant ($P > 0.05$) (Supplementary Table 2 and Supplementary Fig. 5; details in Supplementary Note 3). XPS does not allow microscopic imaging and the X-ray (10–400 μm beam size) cannot focus on the etching area to resolve the chemical modifications of PDMS, thus demonstrating a further advantage of O-PTIR.

Depth-resolved O-PTIR imaging allowed us to reveal the mechanism underlying the evolution of the etching area during steaming. The defocusing caused by the height difference between objects ($\Delta h \pm 5$ μm in the z direction) leads to an obvious signal attenuation in the respective visible-laser and O-PTIR images (for example, as seen in the image of a 10 μm polymethyl methacrylate sphere on the silicone-rubber substrate; Supplementary Fig. 6, details in Supplementary Note 4). Conversely, the strong contrast in the images of objects in and out of focus plane indicates a $\Delta h > 5$ μm between the objects. In the O-PTIR images at 1,263 cm^{-1} (Si–CH_3 band of PDMS) (Fig. 2d), the IR absorption intensity of the etching area clearly differed from that of the bulk rubber, demonstrating that the etching area was separated from the surface of bulk rubber by >5 μm in the z direction (their relative positions are shown schematically in Fig. 2e). Defects on the teat subsample surface may have promoted the diffusion of oxygen and water vapour into the silicone-rubber surface[38,39] during the first 10 min of steaming, with the pressure difference between the internal and external gases causing polymer expansion such that the etching area bulged out over the bulk rubber. In subsequent steam treatments, the etching area cracked, released gases and caved into the bulk rubber to a depth of >5 μm.

The O-PTIR imaging also revealed notable changes in the molecular structure of the PA resins. The optical images (Fig. 2a) showed that the resin particles could detach from or re-attach to the teat subsample surface during the alternating steaming and washing steps. A comparison of the contours of the same resin par-

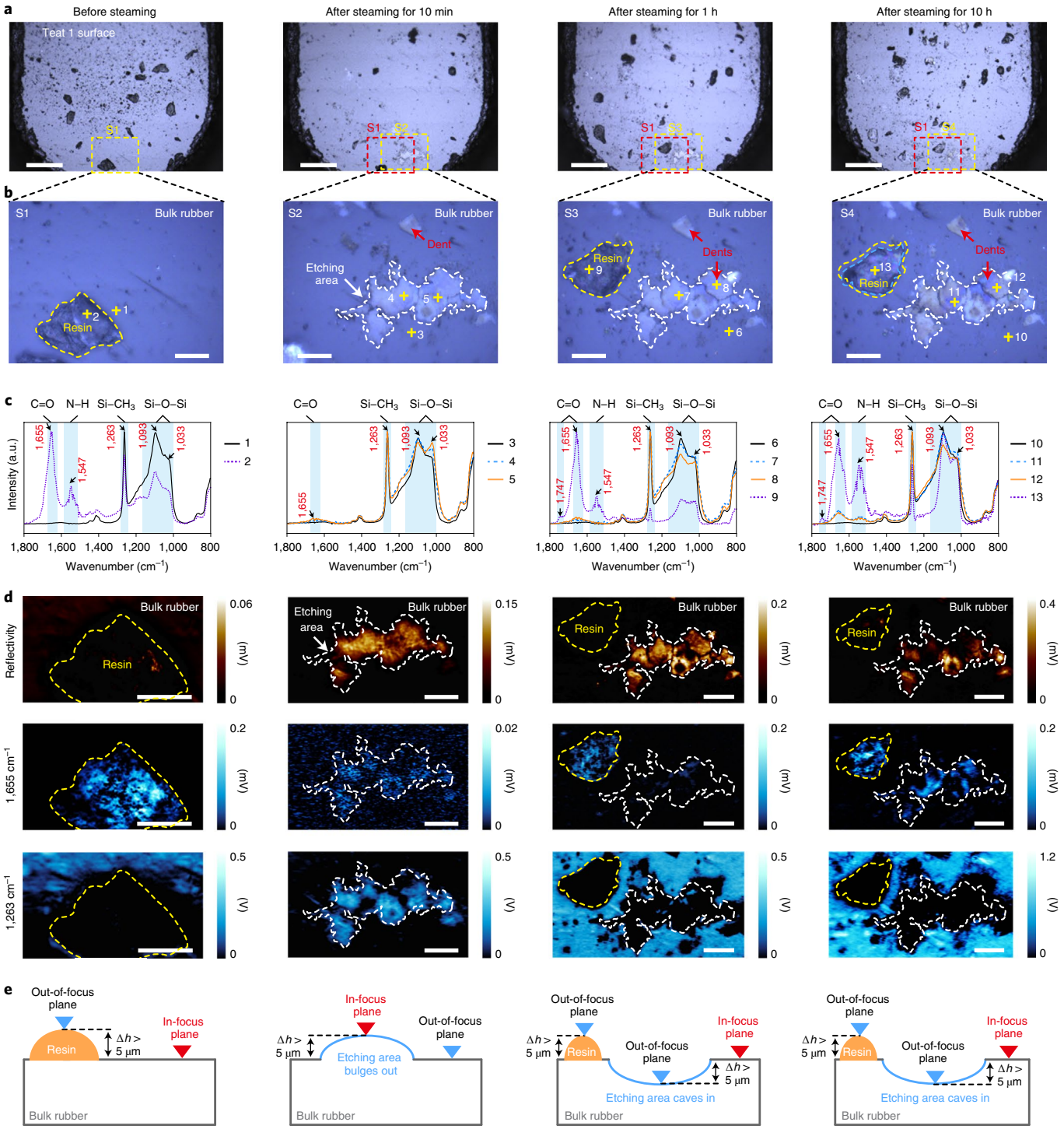

Fig. 2 | Visualization of the evolution of etching on teat surface. a, Optical images of one location on the teat 1 subsample surface before and 10, 60 and 600 min after steaming. Scale bars, 100 μm. **b**, Magnified images of the boxed regions (S1–S4) shown in **a**. Region S1, with 64.7% of the area overlapping with that of S2–S4, was randomly imaged to show the original morphology of the bulk-rubber and resin particles before steaming. Etching areas are enclosed by the white dashed lines. Scale bars, 20 μm. **c**, Normalized O-PTIR spectra of positions 1–13 in **b**. **d**, Visible-laser and O-PTIR images of C=O (1,655 cm^{-1}) and Si–CH_3 (1,263 cm^{-1}) groups in partial areas of the regions S1–S4 shown in **b**, acquired at a resolution of 200 nm per point, a rate of 1,000 μm s^{-1}, a visible-laser power of 9%, an IR power of 8% and a detector gain of 2×. The colour scales show the signal intensity. Scale bars, 20 μm. **e**, Schematic of the positions of the focus planes, where the images in **d** were acquired, and the morphological evolution of the etching areas on the teat surface.

ticle after 1 and 10 h of steaming (Fig. 2b, blue versus yellow lines in S4) showed that shrinkage had occurred. This detachment and shrinkage of the resins indicated the decomposition of the PA and/or PDMS–PA polymer blends. For the same resin particle (Fig. 2c, points 9 and 13), the reduced absorption intensity at 1,655 versus 1,547 cm^{-1} (amide I and II bands, respectively) could be attributed to C–N bond cleavage of PA[40], with the formation of a new C=O band at 1,747 cm^{-1} resulting from PA oxidation.

Formation of polysiloxane-containing particles (type I MNPs) due to decomposition of the base PDMS elastomer

Steam releasing MNPs from silicone teats was first tested by weighing individual whole teats (nos. 1–4) before and after steaming and the particles presented in their wash waters. The wash waters of the same teats were filtered through the same 20 nm Al_2O_3 membranes, which were then air dried and weighed (Fig. 1a). There was no significant ($P > 0.05$) weight loss or gain for either the steamed teats or the membranes (Supplementary Table 3), whereas a large number of microflakes were found in the dried wash waters of all steamed teats (Fig. 3a). The microflakes were generated by steaming, as they were not visible in the dried wash waters of the non-steamed teats (Supplementary Fig. 7). Their different layer numbers (1–3) and colours (for example, pink, yellow and brown) in the optical images (Supplementary Fig. 8a)—a result of white light interference when propagating through the transparent particles—indicated that they were very thin and differed in thickness[41]. Environmental scanning electron microscopy (ESEM) and energy-dispersive X-ray spectroscopy (EDS) revealed that the microflakes were 255–678 nm thick and composed of similar elements (C, O, Mg, Al and Si; Supplementary Fig. 8), with their Mg and Al components probably originating from additives (Mg and Al hydroxides)[42].

As expected, O-PTIR microspectroscopy readily detected the IR absorption signals from the thin microflakes released from steamed teats 1–4. Their O-PTIR spectra were similar (Fig. 3b, points 1–12) but clearly distinct from those of the original PDMS on the non-steamed teats (Fig. 3b). The signal of the Si–CH_3 band (1,263 cm^{-1}) was consistently weaker in the microflakes than in the PDMS, suggesting that either the methyl groups were partially replaced or their signals were masked by newly formed species. The Si–O–Si double bands (1,093 and 1,033 cm^{-1}, Fig. 3b) in the PDMS were replaced by a single Si–O–Si band (1,015–1,003 cm^{-1}, points 1, 4, 7 and 10 in Fig. 3b), a broad band (from 1,160 to 1,000 cm^{-1}, points 3, 6, 9 and 12 in Fig. 3b) or overlapping bands (Fig. 3b, points 2, 5, 8 and 11), indicating the presence of cyclic $[R_2SiO_{2/2}]_3$ and/or branched $[RSiO_{3/2}]_x$ structures in the microflakes[34]. On the basis of the IR absorption at 1,659–1,655 cm^{-1} (C=O stretching vibration), 1,207–1,215 cm^{-1} (C–H rocking and twisting vibrations of the –CH_2– group) and/or 950–810 cm^{-1} (O–H stretching vibration of the Si–OH group) (Fig. 3b, points 1–12), the microflakes probably contained Si–C–C=O, Si–CH_2–CH_2– and/or Si–OH groups[33], respectively. The XPS survey and high-resolution C 1*s* spectra confirmed the significant ($P < 0.05$) difference in surface elemental composition between the microflakes and the non-steamed teats (higher oxygen content in the microflakes) (Supplementary Table 2) and the presence of Si–C and C=O groups on the microflake surfaces (Supplementary Fig. 5 and Supplementary Note 3). XPS detected only a very small percentage of Si ((2.0 ± 0.13)%) on the microflake surfaces at a nanometre-scale sampling depth, but the absence of Si 2*s* or Si 2*p* spectra hampered the identification of Si–O binding at binding energies of 152 and 101 eV. These microflakes with surface-active cyclic and branched polysiloxanes[17] were defined as type I MPs.

With its ability to map large areas at a rate of 1,000 μm s^{-1} in the *x* direction, O-PTIR microspectroscopy enabled determination of the number and size of type I MPs cumulatively collected on the Al_2O_3 filter membranes. Eight areas (each 600 × 500 $μm^2$) on the surface of each membrane were randomly selected (Supplementary Fig. 9, S1–S8) for O-PTIR mapping at 1,010 cm^{-1} (the characteristic Si–O–Si band of type I MPs, Fig. 3b) and a resolution of 500 nm per point (18 min per area). Under these conditions, type I MPs with >1.5 μm in size were distinguished from the membrane substrate in the visible-laser and O-PTIR images (Fig. 3c), amounting to 53–637 particles per area (image). The total amounts of type I MPs released from whole teats following 60 × 10-min steaming events ranged from (0.99 ± 0.25) × 10^5 to (5.0 ± 0.82) × 10^5 particles per teat ($n = 24$) (Fig. 3d), with an average of (2.2 ± 1.7) × 10^5 particles per teat ($n = 96$). The accuracy of particle counting by O-PTIR was verified using polyethylene microspheres, with a comparable recovery ((91 ± 5)%; $n = 3$) to that of Raman microspectroscopy (details in Supplementary Note 5). Overlays of the visible-laser and O-PTIR images allowed differentiation of the contours of individual MPs and measurement of their size (length) in each image (see the example of a 1.7 μm MP in Supplementary Fig. 9). For the four brands of teats, the released MPs (640–4,364 particles counted from eight sampling areas) ranged in size from 1.5 to 332 μm. Classifying the MPs into six size-based groups (Fig. 3e) showed that most ((81 ± 12)%) were 1.5–10 μm in size. O-PTIR mapping performed using a higher resolution (100 nm per point) and laser power identified smaller MPs (roughly 1.4 μm) and NPs (roughly 610 nm) (Fig. 4a) in the wash waters of the steamed teats. Those particles had O-PTIR spectra (Fig. 4b, points 1 and 2) similar to those of the larger MPs (Fig. 3b, points 3, 6, 9 and 12). This study uses O-PTIR to identify NPs, which, as noted above, is not possible with conventional FTIR or Raman microspectroscopy.

The cyclic and branched polysiloxanes identified in the type I MNPs but not found in the original PDMS elastomer (Fig. 3b) suggested that the particles were more reactive than bulk rubber. Single-particle O-PTIR mapping of type I MPs was performed at a resolution of 50 nm per point to test the chemical reactivity of the particles during steaming. The optical images of a randomly selected microflake showed no notable morphological changes before and after 3 h of steaming (Fig. 4c). By contrast, in the O-PTIR images at 1,145 and 1,010 cm^{-1} (the Si–O–Si bands in $[R_2SiO_{2/2}]_3$ and $[RSiO_{3/2}]_x$, respectively) and the ratio maps derived from those images, reductions in the signal intensities of the cyclic and branched polysiloxanes on the particle surface after 3 h of steaming were noted (Fig. 4d). This observation demonstrated the steaming-induced transformation of the polysiloxanes along the basal plane of the particle. It also suggested that the small microplastics (Fig. 4a) likewise originated from the basal plane of the large MPs, due to the decomposition of the polysiloxanes during steaming. The IR absorption bands characteristic of the Si–C–C=O, Si–CH_2–CH_2– and Si–OH groups and $[R_2SiO_{2/2}]_3$ and $[RSiO_{3/2}]_x$ structures, as seen on the type I MNPs, were consistent with cross-linking and oxidation of the side –CH_3 groups as well as the hydrolysis and cyclo-condensation of the main chain ~Si–O–Si~ in the original PDMS elastomer (proposed pathways in Supplementary Figs. 10 and 11, details in Supplementary Note 6).

Formation of polyimides-containing particles (type II MNPs) due to decomposition of the PA resin additive

The decomposition of PA resins observed by O-PTIR (Fig. 2b,c) suggested the formation of thermoplastic MNPs. To explore this possibility, the dried wash water of a steamed whole teat (brand no. 1) on a grid silicon wafer was characterized by O-PTIR. Numerous oil-film-like stains (0.7–10 μm) (Fig. 5a–d) differing from type I MNPs (Figs. 3 and 4) in their morphology and molecular structure were observed. Low-voltage SEM (Fig. 5b) suggested that the stains were aggregates. The appearance of IR absorption bands at 1,743–1,747 cm^{-1} (C=O stretching vibration), 1,457–1,467 cm^{-1} (C–H scissoring vibration of the –CH_2– group and asymmetric C–H bending vibration of the –CH_3 group), 1,375–1,379 cm^{-1} (symmetric C–H bending vibration of the –CH_3 group), 1,267 cm^{-1} (combined C–N stretching and N–H bending vibrations) and 1,161–1,169 cm^{-1} (C–H rocking and twisting vibrations of –CH_2– group) (for example, points 1–3 in Fig. 5c) suggested that the stains contained imide groups (R–CO–NH–CO–R′)[43]. The addition of a drop of deionized (DI) water (20 μl) to the stains for 10 min followed by its removal using a pipette did not cause a visible change in the morphology and molecular structure of the stains, as determined by the optical images (Fig. 5e) and the O-PTIR spectra

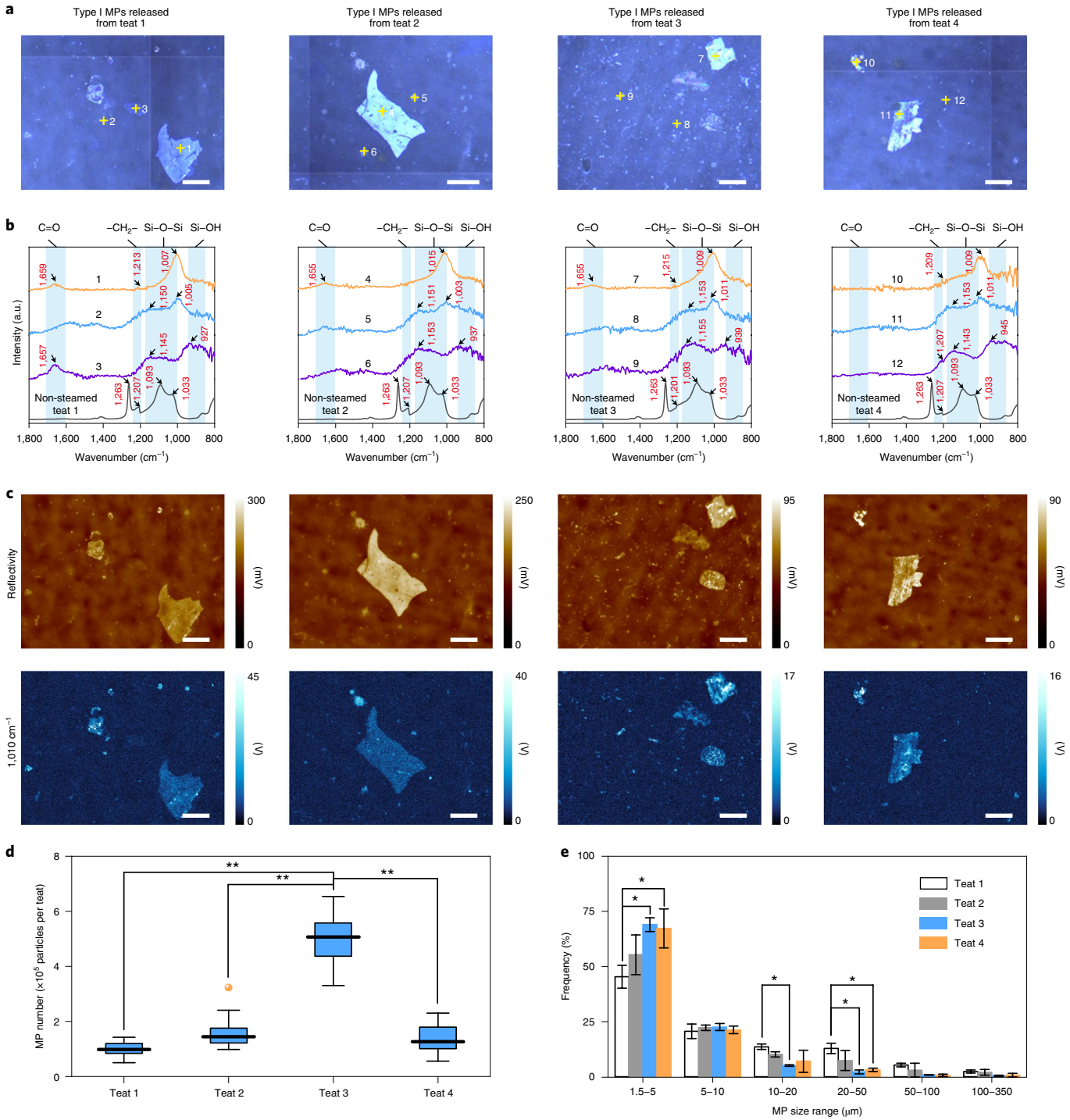

Fig. 3 | Characterization of the molecular structure, number and size distribution of the large PDMS elastomer-derived (type I) MPs. a, Mosaicked optical images of representative MPs on Al_2O_3 filter membranes. The particles were cumulatively collected on the membranes from the wash waters of the teats nos. 1–4 after 60 × 10 min of steaming (Fig. 1a). Scale bars, 50 μm. **b**, Normalized O-PTIR spectra of positions 1–12 in **a**. The O-PTIR spectra of the non-steamed teats were identical to those taken at positions 1, 5, 9 and 13 in Fig. 1b. **c**, Visible-laser and O-PTIR (1,010 cm^{-1}, Si–O–Si group) images of the same areas shown in **a**. The images were acquired at a resolution of 500 nm per point, a rate of 1,000 μm s^{-1}, a visible-laser power of 5%, an IR power of 8% and a detector gain of 2×. The colour scales show the signal intensity. Scale bars, 50 μm. **d**,**e**, Number (**d**) and size distribution (**e**) of the MPs. The MP numbers are presented as box plots (centre line, median; box limits, upper and lower quartiles; whiskers, 1.5× interquartile range; points, outliers), calculated from 24 sampling areas of three replicated membranes. Statistically significant differences were determined using ANOVA and Tukey's test; $^*P < 0.05$, $^{**}P < 0.01$.

(points 3 and 4 in Fig. 5c), indicating that the stains could not dissolve rapidly in DI water at room temperature. In the O-PTIR images at 1,747 cm^{-1}, there was also no change in the size of the stains after water immersion; for example, the particles in region S3 and S4 were both roughly 1.7 μm in size (Fig. 5e). The stains were designated as type II MNPs. They were more heat-labile than the

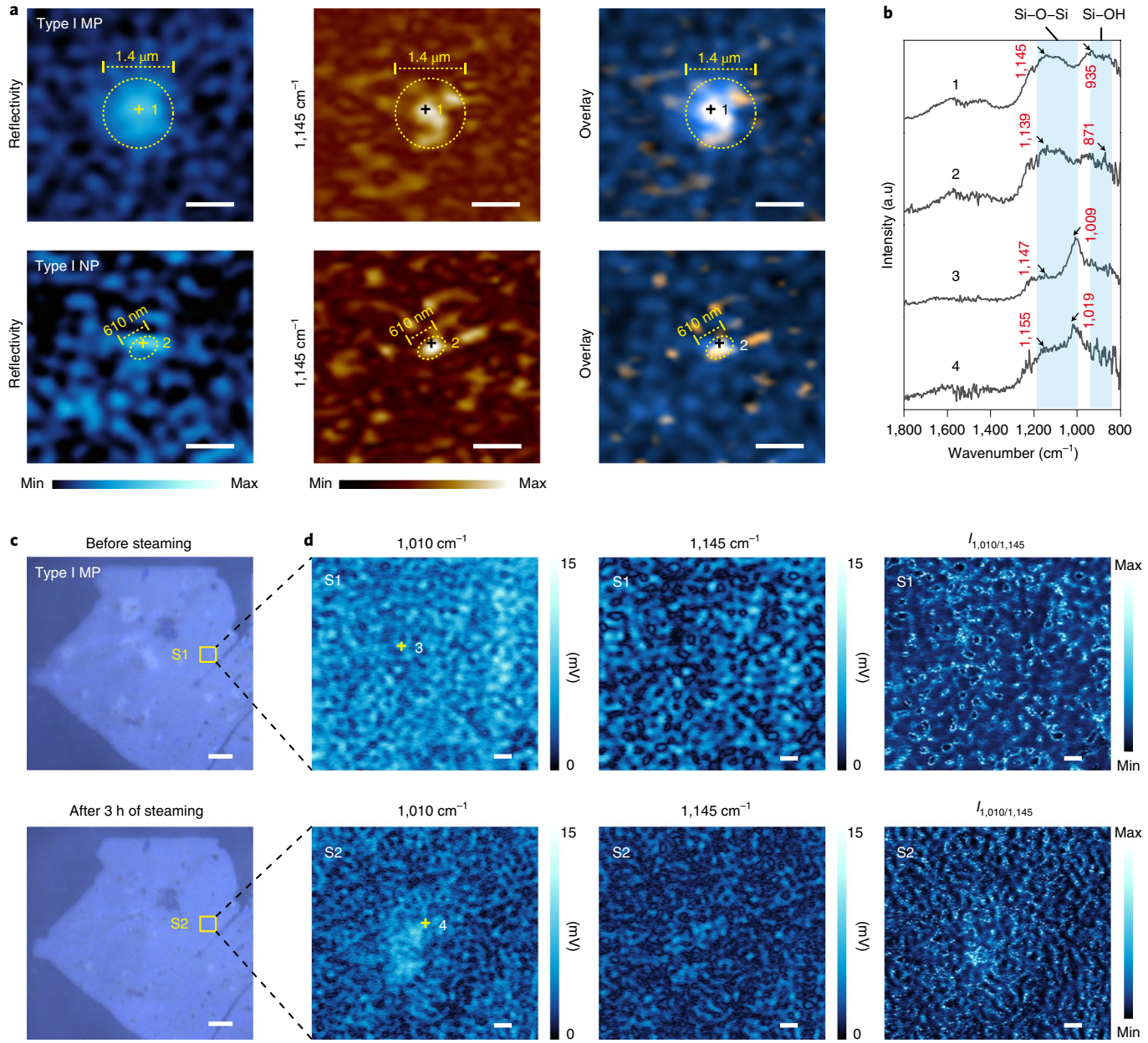

Fig. 4 | Release of small type I MNPs (<1.5 μm) and hydrothermal stability of a larger MP during steaming. a, Visible-laser, O-PTIR (at 1,145 cm^{-1}, Si–O–Si band) and their overlaid images of a representative small MP (roughly 1.4 μm) and NP (roughly 610 nm). The particles were collected on Al_2O_3 filter membranes from the wash water of teat 1 during 60 × 10 min of steaming. Scale bars, 1 μm. **b**, O-PTIR spectra of positions 1–4 shown in **a** and **d**. **c**, Optical images of the same region on a single MP surface before and after 3 h of steaming. Scale bars, 10 μm. **d**, O-PTIR (at 1,010 and 1,145 cm^{-1}, the absorption bands for cyclic $[R_2SiO_{2/2}]_3$ and branched $[RSiO_{3/2}]_x$ structures, respectively) images of boxed areas S1 and S2 in **c** and the ratio maps derived from the O-PTIR images (1,010 versus 1,145 cm^{-1}). The visible-laser and O-PTIR images in **a** and **d** were acquired at the same rate (10 μm s^{-1}) and detector gain (2×) but at different resolutions (100 and 50 nm per point, respectively), IR powers (17 and 8%, respectively) and visible-laser powers (9 and 5%, respectively). The colour scales in the images show the signal intensity. Scale bars, 1 μm.

type I MNPs, since steaming the silicon wafer for 1 min resulted in redistribution of the stains (Fig. 5e), for example, disappearance of the stains (region S3, Fig. 5f). The O-PTIR spectra of the newly formed stains were similar to those of the original stains (point 5 versus point 3 in Fig. 5c), indicating that the type II MNPs melted at 100 °C and could solidify after drying at room temperature, which suggested the random disintegration and aggregation of the type II MNPs on the surface of the steamed teats during steaming and air drying, and therefore we did not count these particles. The presence of the amide II band around 1,547 cm^{-1} (N–H in-plane bending) (for example, points 3–5 in Fig. 5c), one of the characteristic bands of the PA resins both on the teat surface (for example, points 2, 6, 10 and 14 in Fig. 1b,c) and in the wash water (Supplementary Fig. 12), indicated that the type II MNPs originated from the resins as chain scission and oxidation products of the PA polymer (proposed pathways in Supplementary Fig. 13, details in Supplementary Note 6). The polyimide molecules (that is, ~CH_2–CO–NH–CO–CH_2~) comprised the type II MNPs. PA decomposition could cause the linkages at the resin–silicone-rubber interface to break, leading to resin detachment or shrinkage (Fig. 2b).

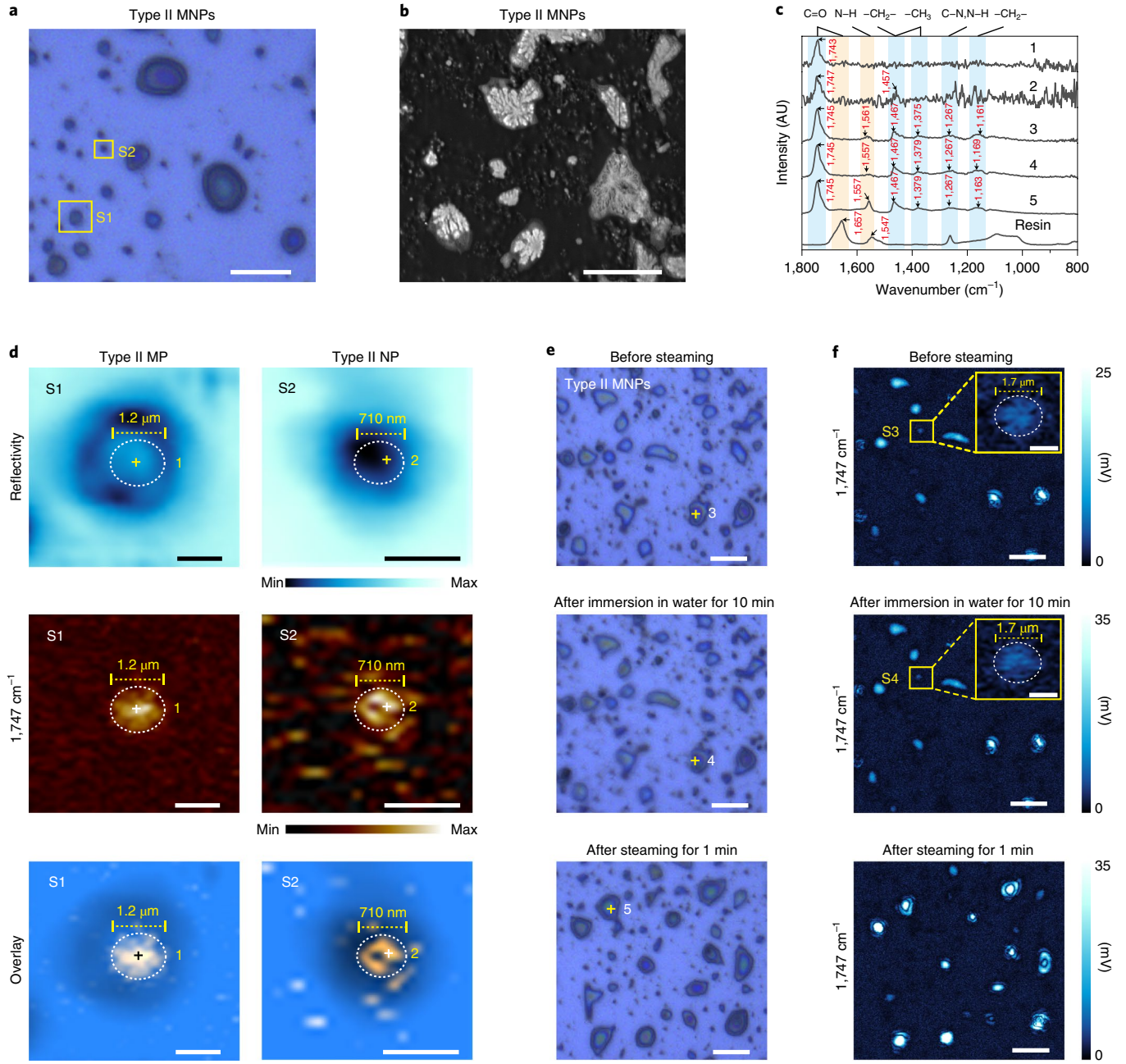

Fig. 5 | Characterization of the morphology and molecular structures of PA-additive-derived (type II) MNPs. a,**b**, Optical (**a**) and SEM (**b**) images of representative type II MNPs, collected from the wash waters of teat 1 after 6 × 10 min of steaming. Scale bars 10 μm (**a**) and 5 μm (**b**). **c**, O-PTIR spectra at positions 1–5 in **d** and **e**. The O-PTIR spectrum of the resin was taken at position 2 in Fig. 1b. **d**, Visible-laser, O-PTIR (at 1,747 cm^{-1}, carbonyl group) and their overlaid images of the MNPs in regions S1 and S2, boxed in **a**. Scale bars, 1 μm. **e**,**f**, Optical (**e**) and O-PTIR (**f**) (1,747 cm^{-1}) images of representative type II MNPs. The images were taken at the same area on the silicon wafer surface before and after immersion of the wafer in DI water for 10 min and after steaming for 1 min. Insets show enlarged images of regions S3 and S4 (scale bars, 1 μm). The images in **d** and **e** were taken at the same resolution (100 nm per point), IR power (17%) and detector gain (2×) but at different rates (10 and 1,000 μm s^{-1}, respectively) and visible-laser powers (9 and 5%, respectively). The colour scales show the signal intensity. Scale bars in **e** and **f**, 10 μm.

Per capita intake and emission of MPs from silicone teats

The release of MNPs during the steam disinfection of silicone teats indicates the direct exposure of bottle-fed infants to surface-active small particles. We estimated that the potential intake dose of type I MPs for an infant during the bottle-feeding period (birth to 18 months) could be $(1.0 \pm 0.75) \times 10^6$ particles (details in Supplementary Note 7). By the age of 1 year, an infant could ingest $(0.66 \pm 0.51) \times 10^6$ MPs of such type. This amount is approximately one order of magnitude higher than the estimated annual intake of thermoplastic microplastics by children (0.07×10^6 particles from the microplastic-contaminated air, water and food[6], but two orders of magnitude lower than that released from the polypropylene feeding bottles[9]. Thus, the elastomer-derived MPs (and even NPs) from the steam-disinfected silicone teats are an important contribution of another different type of MNP to the microplastic exposure of children <18 months of age. The MNPs generated during the moist heat disinfection of silicone teats also contribute to microplastic pollution in the environment. We estimated

that an annual global emission of type I MPs from teat disinfection would be $(5.2 \pm 4.0) \times 10^{13}$ particles, with an annual emission of $(1.3 \pm 1.0) \times 10^{6}$ MPs per bottle-fed infant; annually, discarded teats generate 3.6 ± 1.3 kilotons of silicone waste (details in Supplementary Note 7). The actual intake dose and global emission of MPs derived from silicone teats may be much higher than our estimates, because the estimation took into account only the type I MPs, and the damage to teats caused by intensive disinfection and infant biting may generate far more particles (more discussion in Supplementary Note 7). Our study quantitatively assesses human direct exposure to elastomer-derived MPs during the use of silicone-rubber-based consumer products.

The risks to infant and environmental health posed by the cyclic and branched polysiloxane- or polyimide-containing MNPs are as yet unknown. Although we did not examine their toxicity, adverse effects of small thermoplastic (for example, PS and PET) microplastics have been reported in simulated human gastrointestinal systems[44–46] and in animal models[47–50]. NPs of PS and PET could absorb on intestinal epithelia and thus disrupt nutrient absorption[46,50]. The interactions of small PS MPs with lipids and digestive enzymes could also affect lipid digestion and absorption in the gut[45], which could lead to deficiencies in essential fats and fatty acids in infants[51]. Exposure of intestinal cells and gut microbes to such PS MPs could result in cell dysfunction[49] or microbiota dysbiosis[47,49], both of which are associated with higher risks of developing inflammatory diseases and metabolic disorders[52,53]. Nonetheless, the findings from thermoplastic MNPs cannot be simply extrapolated to the silicone-teat-derived MNPs, as biological responses to different types of particle may differ, determined by the physicochemical properties of the particles (for example, shape, size, flexibility and surface chemistry)[5]. Thus, further studies are required to determine the adverse effects of the MNPs released from silicone teats on infant and environmental health.

Conclusion

We successfully used O-PTIR microspectroscopy to identify small microplastics down to 600 nm to demonstrate the formation of cyclic and branched polysiloxane- or polyimide-containing MNPs during the steam disinfection of silicone teats, and to quantify the direct exposure of bottle-fed infants to surface-active MPs during the most vulnerable period of human life. Similarly, MNPs are also likely to originate from other silicone-rubber-based consumer products (for example, bakeware, foldable electric kettles and sealing rings in cups and cooking appliances) heated at temperatures $\geq$100 °C. Attention should thus be paid to the hydrothermal stability of both the base silicone rubber and the polymeric additives used in those products. Our study also identified a previously ignored but important source of MNPs entering the environment. The hydrothermal decomposition of PDMS and PA during steaming endows the surfaces of the MNPs with different properties, which may hinder the detection and identification of the particles in environmental matrices. Further research is needed to investigate the effects of these surface-active MNPs on environmental and human health.

Online content

Any methods, additional references, Nature Research reporting summaries, source data, extended data, supplementary information, acknowledgements, peer review information; details of author contributions and competing interests; and statements of data and code availability are available at https://doi.org/10.1038/s41565-021-00998-x.

Received: 19 November 2020; Accepted: 6 September 2021;
Published online: 11 November 2021

References

1. Rochman, C. M. & Hoellein, T. The global odyssey of plastic pollution. *Science* **368**, 1184–1185 (2020).
2. Pabortsava, K. & Lampitt, R. S. High concentrations of plastic hidden beneath the surface of the Atlantic Ocean. *Nat. Commun.* **11**, 4073 (2020).
3. Isobe, A., Iwasaki, S., Uchida, K. & Tokai, T. Abundance of non-conservative microplastics in the upper ocean from 1957 to 2066. *Nat. Commun.* **10**, 417 (2019).
4. Rillig, M. C. & Lehmann, A. Microplastic in terrestrial ecosystems. *Science* **368**, 1430–1431 (2020).
5. Vethaak, A. D. & Legler, J. Microplastics and human health. *Science* **371**, 672–674 (2021).
6. Cox, K. D. et al. Human consumption of microplastics. *Environ. Sci. Technol.* **53**, 7068–7074 (2019).
7. Zhang, Q. et al. A review of microplastics in table salt, drinking water, and air: direct human exposure. *Environ. Sci. Technol.* **54**, 3740–3751 (2020).
8. Hernandez, L. M. et al. Plastic teabags release billions of microparticles and nanoparticles into tea. *Environ. Sci. Technol.* **53**, 12300–12310 (2019).
9. Li, D. et al. Microplastic release from the degradation of polypropylene feeding bottles during infant formula preparation. *Nat. Food* **1**, 746–754 (2020).
10. Song, Y. K. et al. Horizontal and vertical distribution of microplastics in Korean coastal waters. *Environ. Sci. Technol.* **52**, 12188–12197 (2018).
11. Hartmann, N. B. et al. Are we speaking the same language? Recommendations for a definition and categorization framework for plastic debris. *Environ. Sci. Technol.* **53**, 1039–1047 (2019).
12. Clarson, S. J. *Advances in Silicones and Silicone-Modified Materials* (American Chemical Society, 2010).
13. Clarson, S. J. *Synthesis and Properties of Silicones and Silicone-Modified Materials* (American Chemical Society, 2003).
14. *How to Prepare Formula for Bottle-Feeding at Home* (WHO, 2007).
15. Fromme, H. et al. Siloxane in baking moulds, emission to indoor air and migration to food during baking with an electric oven. *Environ. Int.* **126**, 145–152 (2019).
16. Helling, R., Kutschbach, K. & Joachim Simat, T. Migration behaviour of silicone moulds in contact with different foodstuffs. *Food Addit. Contam. A* **27**, 396–405 (2010).
17. Rücker, C. & Kümmerer, K. Environmental chemistry of organosiloxanes. *Chem. Rev.* **115**, 466–524 (2015).
18. Polyamide resin series developed by General Mills. *Chem. Eng. News* **41**, 58–61 (1963).
19. ter Halle, A. et al. Understanding the fragmentation pattern of marine plastic debris. *Environ. Sci. Technol.* **50**, 5668–5675 (2016).
20. Dawson, A. L. et al. Turning microplastics into nanoplastics through digestive fragmentation by Antarctic krill. *Nat. Commun.* **9**, 1001 (2018).
21. Min, K., Cuiffi, J. D. & Mathers, R. T. Ranking environmental degradation trends of plastic marine debris based on physical properties and molecular structure. *Nat. Commun.* **11**, 727 (2020).
22. Landrigan, P. J., Kimmel, C. A., Correa, A. & Eskenazi, B. Children's health and the environment: public health issues and challenges for risk assessment. *Environ. Health Perspect.* **112**, 257–265 (2004).
23. Song, Y. K. et al. A comparison of microscopic and spectroscopic identification methods for analysis of microplastics in environmental samples. *Mar. Pollut. Bull.* **93**, 202–209 (2015).
24. Ivleva, N. P., Wiesheu, A. C. & Niessner, R. Microplastic in aquatic ecosystems. *Angew. Chem. Int. Ed.* **56**, 1720–1739 (2017).
25. Nguyen, B. et al. Separation and analysis of microplastics and nanoplastics in complex environmental samples. *Acc. Chem. Res.* **52**, 858–866 (2019).
26. Bassan, P. et al. Resonant mie scattering in infrared spectroscopy of biological materials – understanding the 'dispersion artefact'. *Analyst* **134**, 1586–1593 (2009).
27. Chan, K. L. A. & Kazarian, S. G. New opportunities in micro- and macro-attenuated total reflection infrared spectroscopic imaging: Spatial resolution and sampling versatility. *Appl. Spectrosc.* **57**, 381–389 (2003).
28. Koenig, J. L. *Microspectroscopic Imaging of Polymers* (American Chemical Society, 1998).
29. Zhang, D. et al. Depth-resolved mid-infrared photothermal imaging of living cells and organisms with submicrometer spatial resolution. *Sci. Adv.* **2**, e1600521 (2016).
30. Klementieva, O. et al. Super-resolution infrared imaging of polymorphic amyloid aggregates directly in neurons. *Adv. Sci.* **7**, 1903004 (2020).
31. Lo, M., Marcott, C., Kansiz, M., Dillon, E. & Prater, C. Sub-micron, non-contact, super-resolution infrared microspectroscopy for microelectronics contamination and failure analyses. In *Proc. IEEE International Symposium in the Physical and Failure Analysis of Integrated Circuits* 1–4 (IEEE, 2020).
32. Diem, M., Romeo, M., Boydston-White, S., Miljkovic, M. & Matthaus, C. A decade of vibrational micro-spectroscopy of human cells and tissue (1994-2004). *Analyst* **129**, 880–885 (2004).

33. Danilov, V., Wagner, H. & Meichsner, J. Modification of polydimethylsiloxane thin films in H_2 radio-frequency plasma investigated by infrared reflection absorption spectroscopy. *Plasma Process. Polym.* **8**, 1059–1067 (2011).
34. Launer, P. J. & Arkles, B. *Silicon Compounds: Silanes and Silicones* (Gelest, 2008).
35. Park, E. S., Ro, H. W., Nguyen, C. V., Jaffe, R. L. & Yoon, D. Y. Infrared spectroscopy study of microstructures of poly(silsesquioxane)s. *Chem. Mater.* **20**, 1548–1554 (2008).
36. Song, Y. K. et al. Combined effects of UV exposure duration and mechanical abrasion on microplastic fragmentation by polymer type. *Environ. Sci. Technol.* **51**, 4368–4376 (2017).
37. Larson, G. L., Hernandez, D., Montes de Lopez-Cepero, I. & Torres, L. E. The chemistry of alpha-silyl carbonyl compounds. 11. Reaction of alpha-silyl esters with grignard reagents: a synthesis of beta-keto silanes and ketones. Preparation of the douglas fir tussock moth pheromone. *J. Org. Chem.* **50**, 5260–5267 (1985).
38. Charati, S. G. & Stern, S. A. Diffusion of gases in silicone polymers: molecular dynamics simulations. *Macromolecules* **31**, 5529–5535 (1998).
39. Heo, Y. S. et al. Characterization and resolution of evaporation-mediated osmolality shifts that constrain microfluidic cell culture in poly(dimethylsiloxane) devices. *Anal. Chem.* **79**, 1126–1134 (2007).
40. Skrovanek, D. J., Painter, P. C. & Coleman, M. M. Hydrogen bonding in polymers. 2. Infrared temperature studies of nylon 11. *Macromolecules* **19**, 699–705 (1986).
41. Patsyk, A., Sivan, U., Segev, M. & Bandres, M. A. Observation of branched flow of light. *Nature* **583**, 60–65 (2020).
42. Hamdani, S., Longuet, C., Lopez-Cuesta, J. & Ganachaud, F. Calcium and aluminium-based fillers as flame-retardant additives in silicone matrices. I. Blend preparation and thermal properties. *Polym. Degrad. Stabil.* **95**, 1911–1919 (2010).
43. Bartels, T. T. The Sadtler handbook of infrared spectra. *J. Chromatogr. Sci.* **16**, 21A (1978).
44. Stock, V. et al. Uptake and effects of orally ingested polystyrene microplastic particles in vitro and in vivo. *Arch. Toxicol.* **93**, 1817–1833 (2019).
45. Tan, H., Yue, T., Xu, Y., Zhao, J. & Xing, B. Microplastics reduce lipid digestion in simulated human gastrointestinal system. *Environ. Sci. Technol.* **54**, 12285–12294 (2020).
46. Magrì, D. et al. Laser ablation as a versatile tool to mimic polyethylene terephthalate nanoplastic pollutants: characterization and toxicology assessment. *ACS Nano* **12**, 7690–7700 (2018).
47. Luo, T. et al. Maternal polystyrene microplastic exposure during gestation and lactation altered metabolic homeostasis in the dams and their F1 and F2 offspring. *Environ. Sci. Technol.* **53**, 10978–10992 (2019).
48. Jacob, H., Besson, M., Swarzenski, P. W., Lecchini, D. & Metian, M. Effects of virgin micro- and nanoplastics on fish: trends, meta-analysis, and perspectives. *Environ. Sci. Technol.* **54**, 4733–4745 (2020).
49. Gu, W. et al. Single-cell RNA sequencing reveals size-dependent effects of polystyrene microplastics on immune and secretory cell populations from zebrafish intestines. *Environ. Sci. Technol.* **54**, 3417–3427 (2020).
50. Mahler, G. J. et al. Oral exposure to polystyrene nanoparticles affects iron absorption. *Nat. Nanotechnol.* **7**, 264–271 (2012).
51. Barness, L. A. The importance of fats and fatty acids in infant nutrition. *Curr. Med. Res. Opin.* **4**, 28–32 (1976).
52. Clemente, JoseC. et al. The impact of the gut microbiota on human health: an integrative view. *Cell* **148**, 1258–1270 (2012).
53. Nowarski, R., Jackson, R. & Flavell, R. A. The stromal intervention: regulation of immunity and inflammation at the epithelial-mesenchymal barrier. *Cell* **168**, 362–375 (2017).

Methods

Material pretreatments. Silicone baby bottle teats of four popular, commercially available brands were purchased from a Chinese domestic market. The brand names were replaced with number codes (nos. 1–4). The new teats were washed with DI water, air dried and weighed on an analytical balance (0.1 mg readability; BSA124S-CW, Sartorius) before use. MNPs released from the silicone teats were collected on Al_2O_3 filter membranes (20 nm pore size and 25 mm diameter; Anodisc, Whatman), previously prepared by drawing a 16-square grid ($4\times4\,mm^2$) on the surface of the working area (19 mm diameter) using a waterproof pen (Supplementary Fig. 8). The membranes were then soaked in DI water overnight, washed three times with DI water, air dried in petri dishes and weighed using a micro-analytical balance (0.001 mg readability; WXTS3DU, Mettler Toledo). DI water (18.2 $M\Omega\,cm^{-1}$, 25 °C) was prepared using a water purification system (E-POD, Millipore). Unless otherwise stated, all experiments involving washing and air drying of the teats and membranes and filtering of the wash waters were conducted in an ISO Class 7 cleanroom (≥0.5 µm, 3.5×10^5 particles per m^3) to minimize airborne particulate contamination.

Teat and micro(nano)plastic sample preparations. To investigate polymer decomposition on the teats and the consequent release of MNPs during steam disinfection, three whole teats from each brand (nos. 1–4) were placed in clean glass petri dishes, which were then transferred to a stainless-steel steamer containing boiling DI water (Fig. 1a). The dishes were suspended above the water level to avoid direct wetting. The initial water volume was 30% of the steamer's volume. The steamer was covered and the water was kept at 100 °C for up to 10 h. After a 10 min of steaming, the teats were removed from the steamer, cooled to room temperature (25 °C), washed three times with 50 ml of DI water and then steamed for a further 10 min. This protocol was repeated 60 times, on the basis of the assumption that a teat is used for 60 consecutive days (as recommended by the manufacturers) and disinfected for 10 min d^{-1} before each use. The wash waters of the same teat were combined and filtered through the pretreated Al_2O_3 filter membrane under vacuum. After the 12th, 24th, 36th, 48th and 60th 10 min of steaming, the teats and membranes were air dried and weighed as described above. After 60×10 min of steaming, the teats were cut into $20\times5\,mm^2$ flat pieces for use in the O-PTIR analysis; MNPs retained on the membranes were directly analysed by O-PTIR microspectroscopy (below). Negative control experiments were performed using three teats of each brand (nos. 1–4) and the same procedures as described above but without the steaming step. Results are shown in Figs. 1, 3 and 4.

Another group of new teats (brand 1) were treated using the steaming and washing procedures described above. Aliquots (2 ml) of the wash water after the first, sixth and 60th steaming were filtered through Al_2O_3 membranes (0.02 µm pore size and 47 mm diameter; Anodisc, Whatman). Type I MNPs retained on the membranes were analysed by light microscopy and SEM–EDS (below). An aliquot (30 µl) of the wash water collected after the sixth 10-min steaming session was air dried on a Pelcotec SFG12 silicon wafer ($12.5\times12.5\,mm^2$ with $1\times1\,mm^2$ grids) or on an adhesive carbon tape to characterize the type II MNPs by O-PTIR or SEM, respectively (below). Negative control experiments were conducted identically but without the steaming step (brand no. 1). Results are shown in Fig. 4 and Supplementary Fig. 8.

Teat subsample hydrothermal decomposition kinetics. To visualize the hydrothermal decomposition of the teat polymer during repeated steaming, subsamples ($5\times5\,mm^2$) cut from a new teat (brand no. 1) were analysed by O-PTIR and then steamed at 100 °C for up to 10 h using the same steaming and washing procedures as used for the whole-teat samples. After each 10 min of steaming, the teat subsamples were removed from the steamer, cooled to room temperature (25 °C), washed three times with DI water, air dried and immediately analysed by O-PTIR. These steps were repeated 60 times. The kinetic experiment was conducted in the laboratory of Quantum Design (Beijing) Co., Ltd, where cleanroom conditions were not available. Negative control experiments were performed identically but without the steaming step. Results are shown in Fig. 2.

O-PTIR microspectroscopy. The teat subsamples (on CaF_2 slide) and MNPs (on Al_2O_3 filter membranes or silicon wafers) were analysed using a mid-IR (1,800–800 cm^{-1}) mIRage microspectroscope (Photothermal Spectroscopy Corp.) through a reflective Schwarzschild objective (×10 or ×40, 0.78 NA, 8 mm working distance). A tunable pulsed four-stage quantum cascade laser device was used as the pump IR source, and a continuous-wave single-frequency 532 nm visible laser provided the probe beam. The quantum cascade laser's four chips covered a frequency range of 1,800–800 cm^{-1}; the laser chip's transition positions were 1,440, 1,204 and 925 cm^{-1}. The optimized IR positions were: 1,740 cm^{-1} (*x* 3.66 µm, *y* 9.06 µm), 1,452 cm^{-1} (*x* 3.87 µm, *y* 8.19 µm), 1,260 cm^{-1} (*x* 3.78 µm, *y* 8.34 µm), 1,020 cm^{-1} (*x* 4.52 µm, *y* 7.19 µm) and 875 cm^{-1} (*x* 2.78 µm, *y* 9.00 µm). The raw O-PTIR spectra were collected at a spot size of roughly 500 nm and a scanning step size of 2 cm^{-1}, and represented the original photothermal amplitude without any manipulations unless otherwise stated. Visible-laser and O-PTIR images were sample-dependently acquired at a resolution of 50–500 nm per point, a rate of 10–1,000 µm s^{-1}, a visible-laser power of 5 or 9%, an IR power of 8 or 17% and a detector gain of 2× or 5×. The O-PTIR spectra were normalized and ratio or overlay maps were produced using PTIR Studio software (v.4.3.7471, Photothermal Spectroscopy Corp.). Imaging of the same regions on the surface of the teat subsamples or MP particles was ensured by locating the sampling areas ($128\times96\,\mu m^2$ or $13\times12\,\mu m^2$, respectively) on the basis of their positions relative to reference objects.

Light microscopy and SEM–EDS. Type I MPs retained on the Al_2O_3 membranes were morphologically characterized using a light microscope (Novel N-300M, Ningbo Yongxin Optics Co., Ltd) at ×40 magnification and an ESEM (Quanta FEG 250, FEI) coupled to an EDS system (Aztec X-MaxN80, Oxford Instruments). Samples were directly imaged by ESEM (without sputter coating) in low-vacuum mode and at an accelerating voltage of 5 kV. Type II MNPs on adhesive carbon tapes were observed using an electron microscope (LVEM5, Delong America) operating at 5 kV in SEM mode.

Statistical analysis. The $I_{1,033/1,093}$ (disorder index) and $I_{1,655/1,263}$ (carbonyl index) at different sampling points on the teat surface, the dry weights of the teats (before and after steaming) and Al_2O_3 filter membranes (before and after filtering of the wash waters of the teats, that is, without and with MNPs on the membranes, respectively), and the number of MPs released from different brands of teats were analysed in a one-way analysis of variance (ANOVA) followed by a Tukey's test ($^*P<0.05$, $^{**}P<0.01$). All statistical analyses were conducted using SPSS Statistics software (v.17.0, IBM).

Data availability

All data supporting the findings of this study are available within the article and the Supplementary Information. Source data are provided with this paper.

Acknowledgements

This work was supported by the Key-Area Research and Development Program of Guangdong Province (grant no. 2020B1111380003 to R.J.) and the National Natural Science Foundation of China (grant nos. 31861133003 to R.J. and 21607072 to Y.S.). We thank C. Wang (Nanjing University) for his assistance with the IR spectra analysis and M. K. F. Lo (Photothermal Spectroscopy Corp.) for technical support. B.X. acknowledges the UMass Amherst Conti Faculty Fellowship.

Author contributions

Y.S. carried out the experiments and wrote the original manuscript. X.H. and H.T. supported the O-PTIR and low-voltage SEM analyses. K.L. supported ESEM/EDS collection and XPS spectra analysis. H.L. supported MP counting. S.L. contributed to experimental planning and data interpretation. Y.S., B.X. and R.J. contributed to experimental planning, data analysis and interpretation, and manuscript revision. All authors reviewed and approved the paper.

Competing interests

The authors declare no competing interests.

Additional information

Supplementary information The online version contains supplementary material available at https://doi.org/10.1038/s41565-021-00998-x.

Correspondence and requests for materials should be addressed to Baoshan Xing or Rong Ji.

Peer review information *Nature Nanotechnology* thanks Ji-Xin Cheng, Oxana Klementieva and the other, anonymous, reviewer(s) for their contribution to the peer review of this work.